

Designer Monte Carlo Simulation for Gross-Neveu Transition

Yuzhi Liu,^{1,2} Kai Sun,³ and Zi Yang Meng^{4,1,5,6}

¹*Beijing National Laboratory for Condensed Matter Physics and Institute of Physics,
Chinese Academy of Sciences, Beijing 100190, China*

²*School of Physical Sciences, University of Chinese Academy of Sciences, Beijing 100190, China*

³*Department of Physics, University of Michigan, Ann Arbor, MI 48109, USA*

⁴*Department of Physics and HKU-UCAS Joint Institute of Theoretical and Computational Physics,
The University of Hong Kong, Pokfulam Road, Hong Kong, China*

⁵*Songshan Lake Materials Laboratory, Dongguan, Guangdong 523808, China*

⁶*CAS Center of Excellence in Topological Quantum Computation and School of Physical Sciences,
University of Chinese Academy of Sciences, Beijing 100190, China*

(Dated: October 17, 2019)

In this manuscript, we study quantum criticality of Dirac fermions via large-scale numerical simulations, focusing on the Gross-Neveu (GN) chiral-Ising quantum critical point with critical bosonic modes coupled with Dirac fermions. We show that finite-size effects at this quantum critical point can be efficiently minimized via careful model design, which maximizes the ultraviolet cutoff and at the same time places the bare control parameters closer to the nontrivial fixed point to better expose the critical region. Combined with the efficient self-learning quantum Monte Carlo algorithm, which enables non-local update of the bosonic field, we find that moderately-large system size (up to 14×14) is already sufficient to produce robust scaling behavior and critical exponents. The conductance at the QCP is also calculated and its frequency dependence is found to be consistent with the scaling behavior predicted by the conformal field theory. The methods and model-design principles developed for this study can be generalized to other fermionic QCPs as well, and thus provide a promising direction for controlled studies of strongly-correlated itinerant systems.

I. INTRODUCTION

Quantum critical points (QCP) in the presence of fermionic fluctuations are among the most intriguing topics in the study of strongly correlated systems, which pave the way towards new paradigms of quantum matter beyond the conventional Fermi-liquid theory of metal and the Landau-Ginzburg-Wilson theory of phase transitions. Due to the strong coupling nature, to understand these fermionic QCPs remains a highly challenging task, and many fundamental questions remain open. For example, after four decades of intensive studies, quantum criticality in the presence of Fermi surfaces still remains a highly active research subject, from the early effort of the Hertz-Mills-Moriya framework [1–3] based on the leading-order approximation to the more recent studies that reveal the crucial and nontrivial contributions of higher order terms [4–7]. Even today, the fate of such fermionic QCPs still remains an important open question and a source for exciting new ideas and insights [7–10].

The situation at the numeric front is equally, if not more, challenging, as the divergent length scale and the fermionic nature of this problem prevents us from obtaining unbiased and reliable numerical solutions at the thermodynamic limit. For example, in contrast to bosonic QCPs, many of which can be efficiently simulated via quantum Monte Carlo (QMC) methodologies [11], the notorious sign problem makes it highly challenging to access the same level of knowledge in the presence of fermionic fluctuations. Only until very recent, new pathways towards large-scale unbiased simulations of fermionic QCPs become available, where utilizing designers models, various fermionic QCPs become accessible to sign-problem-free QMC simulations, such as nematic [12], ferromagnetic [13] and antiferromagnetic QCPs [14–17] (See Ref. [18] for a re-

cent review). From these efforts, it becomes possible to obtain accurate and reliable information about the scaling behaviors in the close vicinity of these QCPs, for testing and improving our theoretical knowledge about these challenging problems.

In this manuscript, we study fermionic QCPs in strongly-correlated Dirac systems utilizing Gross-Neveu-type models, where interactions between Dirac fermions are mediated by a bosonic field. These QCPs are often referred to as the Gross-Neveu (GN) transitions, which, as will be shown below, can be simulated via sign-problem-free QMC methods. For theoretical treatment, due to the absence of Fermi surfaces and the emergent Lorentz and conformal symmetry, some of the GN QCPs are believed to be among the “simplest” fermionic QCPs, and thus hold the highest expectation for achieving agreement between controlled analytical calculations and numerical simulations. In recent years, such efforts have been attempted from both numerical and theoretical sides, e.g., the chiral-Ising GN transitions have been studied via high-order expansions [19, 20] and quantum Monte Carlo simulations [21–24].

In the numerical studies of GN transitions and its quantum criticality, the most significant challenge lies in the finite-size effect. A typical fermionic quantum Monte Carlo requires a complexity of $O(\beta N^3)$ where $N = L^d$ is the lattice size with L being the linear span of the d dimensional system and β is the inverse temperature. In addition to the typical challenge of critical slowing down, quantum critical points in the GN models have two additional sources of finite-size effects. First, in a lattice model, Dirac fermions emerge in the close vicinity of the Dirac points. As far as critical phenomena are concerned, the part of the energy band near the Dirac point (with linear dispersion) contributes to the correct infrared (IR) scaling behavior, while the rest part of the energy band, which deviates from the Dirac linear dispersion, gives

short-distance non-universal physics. In other words, the scaling behavior comes from only a portion of the Brillouin zone (less than 15% in a typical lattice model as shown below), which effectively reduces the system size by $\sim 85\%$ in numerical simulations and thus significantly amplifies finite-size effects. To enlarge the linear-dispersion region, special models are utilized, such as the SLAC fermion construction in the recent work of Ref. 23. However, such special models often involve infinite-long-range hopping, which makes the system non-local. Secondly, in a typically lattice model with bosons and fermions coupled together, these two types of particles in general have different velocities. This velocity difference explicitly breaks the Lorentz symmetry, and results in a very slow (logarithmic) RG flow of the velocities. Such a slow RG flow requires extremely large system sizes to reach the vicinity of the fixed point, making it very challenge to produce the correct exponents.

In the study of fermionic quantum criticality, to overcome the critical slowing down, various efforts have been made to access larger system sizes, such as the self-learning Monte Carlo (SLMC) [25, 26], which provides more efficient updates, and its momentum space extension (elective momentum ultra-size Monte Carlo EQMC) [16]. These improvements addresses the numerical aspect, and are implemented *a posteriori* to the model design. In this manuscript, we utilize a different approach to reduce the finite-size effect through *a priori* optimizing the model design to better utilize the emergent Lorentz symmetry at the chiral Ising GN transition. In particular, we develop designer model Hamiltonians with two properties: (1) the Dirac linear-dispersion region occupies a larger portion of the Brillouin zone *without sacrificing locality* and (2) the bosons and fermions have the *same velocity* to avoid the slow RG flow. These efforts minimize the finite-size effects mentioned above. Combined with advanced numeric scheme such as SLMC, we show explicitly that finite-size effects are efficiently suppressed in the obtained results, given rise to robust critical exponents. Furthermore, the critical exponents are also consistently verified from the frequency scaling behavior of the conductivity at the QCP, which provides the first set of transport results of fermionic QCP with conformal field theory content.

The rest of the paper is organized in the following structure: in Sec. II the designer model of the $N_f = 8$ chiral Ising GN transition is introduced, as well as the techniques that we utilized to enlarge the linear dispersion region and to match the fermion and boson velocities. In Sec. III, the numerical results are presented, which include the crossing point analysis of the critical exponents (Sec. III A), the measurement of the two velocities at the GN QCP (Sec. III B), and eventually the discussion of the finite frequency conductivity at the GN QCP, as well as the conformal field theory prediction (Sec. III C). Finally in Sec. IV, the conclusions are drawn and few immediate future directions are outlined.

II. DESIGNER MODEL

The designer model is realized by coupling Dirac fermions with dynamical bosonic field [21, 22, 27]. The model is defined on a square lattice shown in Fig. 1, with two bosonic sites and two fermionic sites per unit cell. The bosons acquire an Ising symmetry and the Lagrangian of the system is given as

$$L = L_{\text{Boson}} + L_{\text{Fermion}} + L_{\text{Coupling}} \quad (1)$$

with

$$L_{\text{Boson}} = \sum_p \left[\frac{1}{4} \left(\frac{\partial \phi_p}{\partial \tau} \right)^2 + m \phi_p^2 + \phi_p^4 \right] + \sum_{(p,q)} J_{pq} (\phi_p - \phi_q)^2,$$

$$L_{\text{Fermion}} = \sum_{(i,j),\sigma} \psi_{i,\sigma}^\dagger [(i\partial_\tau - \mu)\delta_{ij} - t_{ij} e^{i\sigma\theta_{ij}}] \psi_{j,\sigma} + h.c., \quad (2)$$

$$L_{\text{Coupling}} = \sum_{\langle\langle i,j \rangle\rangle, \sigma} \lambda_{ij} \phi_p \psi_{i,\sigma}^\dagger \psi_{j,\sigma} + h.c.,$$

where $\psi_{i,\sigma}$ ($\psi_{i,\sigma}^\dagger$) is the fermionic annihilation (creation) operator at the fermionic site i with spin $\sigma = \uparrow$ or \downarrow , and ϕ_p represents the bosonic field at the bosonic site p .

Fig. 1 (a) and (b) shows the fermionic part of the model. The fermionic hopping strength carries a complex phase θ_{ij} . For the nearest-neighbor hopping t_1 and the third-nearest-neighbor hopping between different sublattices t_2 , the phase factor is set to $\pi/4$, which introduces a π -magnetic-flux for each plaquette of the fermion lattice. This tight-binding model gives rise to two Dirac cones at $(\pi, 0)$ and $(0, \pi)$ in the Brillouin zone (BZ). The conventional π -flux model with only t_1 is depicted in Fig. 1 (a), which is the tight-binding model employed in previous studies [21, 22]. The model utilized in this work is shown in Fig. 1 (b), where one additional hopping term t_2 is introduced with $t_2 = t_1/27$. As shown in the right panels of Fig. 1 (a) and (b), this additional hopping term greatly increases the area of the linear dispersion region, denoted by the green contour lines, from 13.7% in (a) to 39.8% in (b) of the entire BZ. Here, this green contour marks momentum points, at which the energy band deviates from the ideal linear dispersion by 5%. It serves as the ultraviolet cutoff (Λ) in the renormalization group (RG) analysis of this Dirac system.

For a critical system, the RG flow is governed by the dimensionless quantity $L\Lambda$, where L is the system size. A larger Λ effectively increases the system size, and thus pushes the system closer to the thermodynamic limit. Similar ideas of increasing the linear dispersion area has been used in another recent QMC study [23], where the linear dispersion region is expanded to the entire BZ via introducing infinite-long-range hopping terms, known as the SLAC fermion model. These long-range hopping terms render the model non-local. In contrast, in the model that we adopted here, although the linear-dispersion region doesn't cover the entire BZ, the Hamiltonian is local with only short-range couplings.

Fig. 1 (c) depicts the full model with circles representing the fermionic sites and squares the bosonic ones. Similar to the fermions, the bosons here also have extended, but local, interactions, denoted as J_1, J_2, J_3 and J_4 from the first-neighbor to the fourth-neighbor couplings respectively. The values of

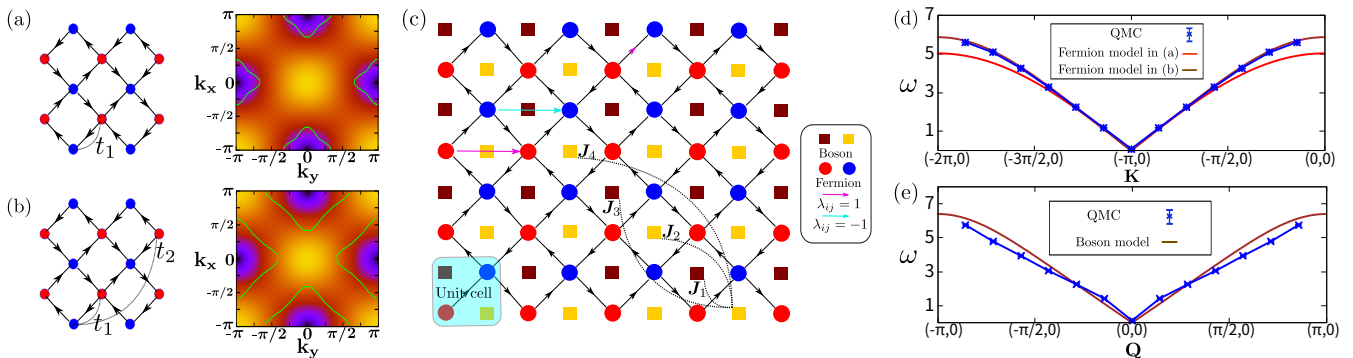


FIG. 1. The fermion tight-binding models are shown in (a) and (b), with (a) only contains the nearest-neighbor hopping t_1 (Ref. [21]) and (b) contain both the nearest-neighbor hopping t_1 and the third-nearest-neighbor hopping between different sublattices t_2 (this work). The green dashed lines in the right panels mark the linear dispersion region, out of which the band structure starts to deviate from the Dirac linear dispersion. The t_2 hopping in Fig. (b) greatly increases the area of the linear dispersion region. The black arrows in the left panel represent the phase of the complex hopping strength $\theta = \frac{\pi}{4}$, and we set $t_1 = 2$ and $t_2 = \frac{t_1}{27}$. The lattice model is depicted in (c), where the coupling constants for bosons are $J_2 = -\frac{J_1}{8}$, $J_3 = \frac{J_1}{63}$, $J_4 = -\frac{J_1}{896}$. The bosons and fermions are coupled together via the $\lambda_{i,j} = \pm 1$ term shown in Eq. (4), where two next-nearest-neighbor fermions are coupled together with the boson between the two fermion sites. The sign of the coupling constant $\lambda_{i,j}$ alternates from one plaquette to another, as marked by in (c). Overall, one unit cell of this model contains two fermion sites and two boson sites. (d) and (e) show dispersions of fermions and bosons respectively. Here, we presented both the bare dispersions (ignoring interactions) and the renormalized ones at the chiral Ising transition via QMC simulations. In Fig. (d), it is easy to notice that model shown in Fig. (b) greatly increases the linear-dispersion region.

these coupling strengths are shown in the caption of Fig. 1. At the QCP, the critical boson mode exhibits a linear dispersion at small wavevector. These values of the J 's maximize the area of this linear-dispersion region, which helps to suppress finite-size effects same as what we did for the fermions above. With this parameter choice, the bare boson velocity at the critical point of L_{Boson} is $v_b = 2\sqrt{5}J_1/8$, and the Fermi velocity at the Dirac point is $v_f = \frac{8}{9}\sqrt{2}t_1$. Here, we set $t_1 = 1$ and choose the value of J_1 such that bosons and fermions share identical velocity $v_b = v_f$ (See Appendix A for details). This identical velocity results in an emergent Lorentz symmetry, where $v_b = v_f$ serves as the speed for light. For a Lorentz-invariant system, it is known that the speed of light would not flow under RG, even in the presence of strong interactions [28]. This *a priori* setup avoids the slow logarithmic RG flow of the velocity mentioned above.

The couplings between bosons and fermions are denoted as λ_{ij} , which couples to a pair of next-nearest-neighbor fermion sites with the boson site between them. The coupling constant λ_{ij} takes the value of ± 1 , where the two bosonic sublattices take opposite signs. In the ordered phase (i.e. the boson field has a nonzero expectation value), this alternating sign gives rise to the required Berry phase to the fermions, and thus gaps out the Dirac points, transforming the Dirac semi-metal into a dynamically-generated quantum-spin-Hall insulator. More details about such a topological phase transition and numerical realization can be found in Ref. [21].

Fig. 1 (d) and (e) depict the dispersions near the fermionic Dirac point at $(\pi, 0)$ and bosonic dispersion at $(0, 0)$ at the QCP. The red and brown lines in (d) are the bare fermion dispersions for the models shown in Fig. 1(a) and (b), respectively. One can see that the linear-dispersion region for the brown line is indeed significantly larger than that of the red line. The

blue stars are the QMC results obtained at the chiral Ising critical point. Fig. 1 (f) presents the bosonic dispersion at the bare Ising critical point (the brown line) and the chiral Ising critical point (the blue stars). It is worthwhile to highlight that for both fermions and bosons, their velocities receive little renormalization. This absence of velocity renormalization is because we set the bosons and fermions to have the same bare velocity as mentioned above.

To solve the model shown in Eq. (1), in particular to obtain its ground state phase diagram and dynamic properties, we employ the projective QMC method [21, 29, 30] with SLMC update schemes. Detailed information of the numeric implementation, in particular on how to obtain accurate effective model in the SLMC within the projective QMC framework, is given in Appendix B.

III. RESULTS

In the simulation, we vary the value of the mass term m in L_{Boson} in Eq. (1). Without fermions, tuning this mass term triggers a $(2+1)$ d Ising transition for the ϕ field. In the presence of the fermions, this transition induces a fundamental change in the fermion band structure. In the disordered (ordered) phase, $\langle \phi \rangle = 0$ ($\langle \phi \rangle \neq 0$), the Dirac fermions is massless (massive), i.e., the long-range order in bosons generates finite mass for the Dirac fermions. In addition, it can be shown that this Dirac mass carry a nontrivial topological index, and results in a dynamically generated quantum spin Hall insulator [21]. Furthermore, the interplay between bosons and fermions also changes the universality of the quantum critical point, from Ising to the GN chiral Ising, which is believed to be among the simplest fermionic QCPs where possibly analytical and

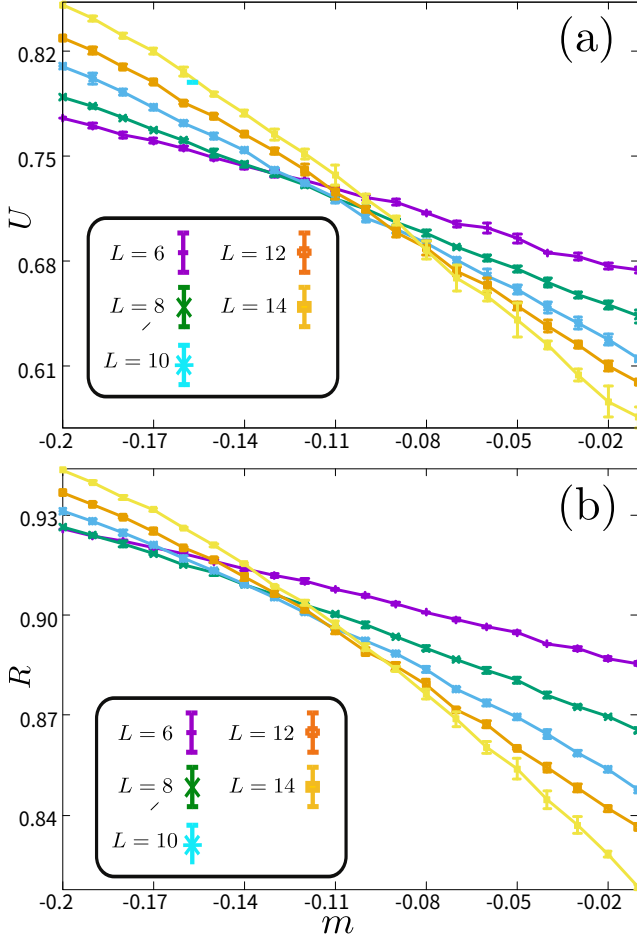


FIG. 2. (a) The Binder ratio $U(L, m)$ for different system sizes L across the transition of m . Curves for two consecutive system sizes L and $L + 2$ cross at the finite size transition point $m_c(L)$. (b) The correlation ratio $R(L, m)$ for different system sizes L across the transition of m . Curves for two consecutive sizes L and $L + 2$ cross at the finite size transition point $m_c(L)$. The finite-size analysis for these crossing points are shown in Fig. 3.

numerical approaches might be able to give consistent critical exponents to build a concrete CFT description [19, 24, 31, 32]. For the model described above, the Dirac fermions acquire $N_f = 8$ flavors, and thus the QCP belongs to the $N_f = 8$ chiral Ising universality class. Below, we reveal step by step how the critical properties of this transition is obtained in our designer QMC simulations.

A. Crossing-point analysis

First we determine the precise location of the quantum critical point via the Binder ratio (U) [33] and correlation ratio (R) [34] of the bosonic order parameter

$$m_\phi^2 = \frac{1}{N} \sum_{\langle p, q \rangle} \phi_p \phi_q \quad (3)$$

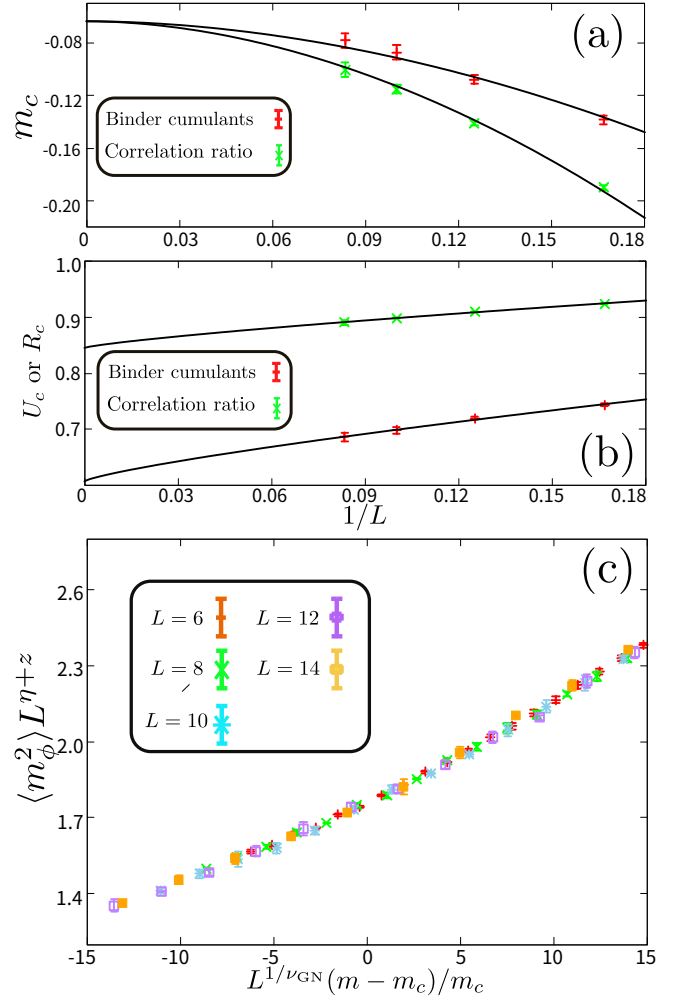


FIG. 3. (a) Crossing point analysis for the Binder and correlation ratios obtained in Fig. 2. The two $m_c(L)$ curves extrapolate to the same critical point $m_c^* = -0.062(3)$ at the thermodynamic limit and the two powers in the extrapolation according to Eq. (6) consistently reveal $1/\nu_{GN} + \omega = 1.8(1)$, with different non-universal coefficients a . (b) Crossing point analysis of the Binder ratio $U_c(L)$ and the correlation ratio $R_c(L)$ according to Eqs. (7) and (8). The obtained correction exponent $\omega = 0.78(6)$. Combining the exponents from Fig. (a) and (b), we find $1/\nu_{GN} = 1.1(1)$. (c) Data collapsing for the order parameter measured at different m and system sizes L . Here, we utilized the the exponent ν_{GN} and the critical point m_c^* obtained above and the system sizes are $L = 6, 8, 10, 12, 14$. A good collapse is achieved with dynamic critical exponent $z = 1$ and the anomalous dimension $\eta = 0.60(2)$.

where N is the number of boson lattice sites, and the two dimensionless ratios are given as

$$U = \frac{3}{2} \left(1 - \frac{1}{3} \frac{\langle m_\phi^4 \rangle}{\langle m_\phi^2 \rangle^2} \right) \quad (4)$$

$$R = 1 - \frac{S(\mathbf{Q} + \delta_{\mathbf{q}})}{S(\mathbf{Q})} \quad (5)$$

here $S(\mathbf{q}) = \frac{1}{N} \sum_{\langle p, q \rangle} e^{-i\mathbf{q} \cdot (\mathbf{r}_p - \mathbf{r}_q)} \phi_p \phi_q$ is the structure factor of the bosonic correlation function and \mathbf{r}_p and \mathbf{r}_q stand for the position of the bosonic field on the lattice. The ordering wavevector in our case is $\mathbf{Q} = (0, 0)$, and $\delta_{\mathbf{q}} = (0, \pi/L)$ or $(\pi/L, 0)$ is the smallest momentum away from \mathbf{Q} on a finite lattice with linear span L .

The results are shown in Fig. 2 (a) and (b). The finite-size transition point $m_c(L)$ is the crossing points of the two consecutive system sizes, and it is clear from the two panels of Fig. 2 that the position of the $m_c(L)$ -s are gradually drifting as L increases. According to the finite size scaling analysis [35, 36], the drift of both the critical point $m_c(L)$ and the corresponding $R_c(L)$ and $U_c(L)$ obey the following scaling behavior at near the critical point,

$$m_c(L) = m_c^* + aL^{-(1/\nu_{\text{GN}} + \omega)}, \quad (6)$$

$$U_c(L) = U_c^* + bL^{-1/\omega}, \quad (7)$$

$$R_c(L) = R_c^* + cL^{-1/\omega}, \quad (8)$$

where ν_{GN} and ω are the correlation length exponent and the correction exponent of the chiral Ising GN transition. m_c^* , U_c^* and R_c^* are critical point, correlation ratio and Binder ratio in the thermodynamic limit and a , b and c are non-universal fitting coefficients.

As shown in Fig. 3(a), the crossing points of different pairs of system size ($L, L+2$) drift towards m_c^* as a power-law function as shown in Eq. (6). It is important to emphasize here that for both the Binder ratio U and the correlation ratio R , the scaling analysis generates the same critical point $m_c^* = -0.062(3)$ and the same critical exponents $1/\nu_{\text{GN}} + \omega = 1.8(1)$. This consistency indicates that finite-size effects are under good control in the current simulation, even though our system sizes are just moderately large.

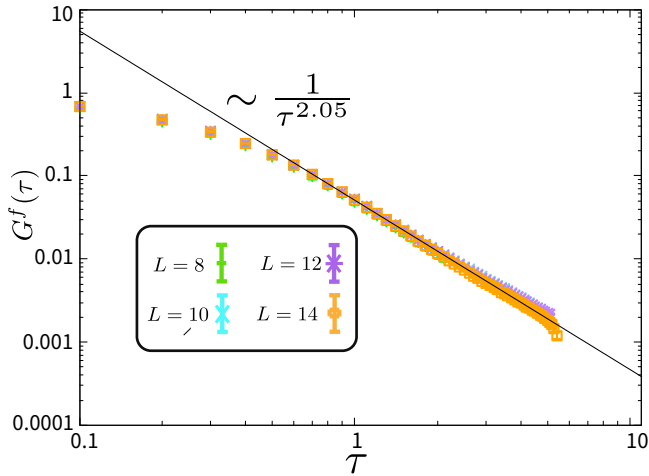


FIG. 4. The imaginary time decay of the fermion Green's function at the chiral Ising QCP. From the power-law decay of $G^f(\tau) \sim 1/\tau^{2+\eta_\psi}$ we obtain the anomalous dimension of the Dirac fermions $\eta_\psi = 0.05(2)$.

In Fig. 3(b), we fit the two curves according to Eqs. (7) and (8), to trace the universal thermodynamic values of the Binder

and correlation ratios U_c^* and R_c^* , as well as the correction exponent ω . It turns out that both the coefficient b and c are positive numbers (In general, their signs depend on the model and could be opposite in certain systems as shown in Ref. [36]), such that both curves decreases as L increases. Interestingly, the two independent fits (for U and R) yields the same same exponent value $\omega = 0.78(6)$. With the value of ω obtained, we can now determine $1/\nu_{\text{GN}} = 1.1(1)$ from the combined exponents in Fig. 3 (a).

With m_c^* , ν_{GN} , we can directly collapse the bosonic order parameter with the universal scaling form $\langle m_\phi^2 \rangle L^{z+\eta} = f(L^{1/\nu_{\text{GN}}}(m - m_c^*)/m_c^*)$. The results are shown in Fig. 3 (c), with $z = 1$ of the $(2+1)$ d chiral Ising universality, the data of $L = 6, 8, \dots, 14$ give a very good collapse and from which we read the bosonic anomalous dimension $\eta_\phi = 0.60(2)$ at the chiral Ising GN QCP.

The fermionic anomalous dimension η_ψ , however, cannot be obtained from the above bosonic crossing analysis but have to be extracted from the fermion Green's function at the QCP. For a QCP with the dynamic critical exponent $z = 1$, there are two ways to obtain this anomalous dimension, by fitting either the time dependence or the spatial dependence of the Green's function, and they should produce the same value. This is indeed what we observed here. However, because the Lorentz symmetry in a lattice model is an emergent symmetry instead of an explicit one, time and space are not fully identical in our model. Thus, although the two fittings produce consistent exponents, the error bars are not the same. For the fermionic anomalous dimension, our simulation indicates that in this model, the time-dependence data has more data points exhibiting power-law behavior and thus allows a more accurate fitting. In Fig. 4, we present the imaginary time decay of the fermion Green's function $G^f(\tau) = \frac{1}{N} \sum_{i=1}^N \langle \psi_{i,\sigma}^\dagger(\tau) \psi_{i,\sigma}(0) \rangle$ at the QCP $m = m_c^*$ and fit the data with its scaling form

$$G^f(\tau) \sim 1/\tau^{2+\eta_\psi}, \quad (9)$$

where the power 2 is the bare-scaling dimension for free Dirac fermions in $(2+1)$ d, and η_ψ accounts for the anomalous part of the exponent at the nontrivial GN fixed point. In Fig. 4, we plot $G^f(\tau)$ at the QCP ($m = m_c^*$) for several system sizes in the log-log scale. It is clear that at large imaginary time, the power-law decay of the fermion Green's function manifests with an anomalous dimension $\eta_\psi = 0.05(2)$.

This completes our analysis of the critical exponents of the $N_f = 8$ chiral Ising GN transition. In Tab. I, we list the obtained critical exponents and compare them with previous QMC works [21, 22] and various high-order perturbative RG results [19, 20] as well as conformal bootstrap estimations [31] (we note here the conformal bootstrap only gives estimation of the exponents based on the position of the kinks from bootstrap calculations [31, 32], the exact value of the exponents within conformal bootstrap analysis for the fermion GN transitions are yet to be obtained).

Two points are in order concerning the obtained exponents in this work in comparison with previous numerical studies. First, in the previous works, in particular the QMC works, finite-size effects have not been reduced as much as in the

	$1/\nu_{GN}$	η_ϕ	η_ψ	ω
This work	1.1(1)	0.60(2)	0.05(2)	0.78(6)
previous QMC [21]	1.2(1)	0.65(3)		
previous QMC [22]	1.20(1)	0.62(1)	0.38(1)	
perturbative RG 4- ϵ loop, Padé [19]	0.931	0.7079	0.0539	0.794
perturbative RG 4-loop, interpolation between 2+ ϵ and 4- ϵ [20]	1.004	0.735	0.042	
bootstrap estimation [31]	0.88	0.742	0.044	

TABLE I. Comparison of obtained critical exponents for the $N_f = 8$ chiral Ising GN universality class. The results are obtained from QMC simulations, 4-loop perturbative RG and the estimate of conformal bootstrap bound. ν_{GN} is the correlation length exponent, η_ϕ is the anomalous dimension of the bosonic field, η_ψ is the anomalous dimension of the fermionic field and ω is the correction exponent in the bosonic sector.

current designer Hamiltonian, i.e., the fermion and boson velocities may not be the same at the bare level and the RG flow might not be able to synchronize them limited by the finite system size, whereas in the present case, the $v_f = v_b$ *a priori* and as will be shown in the next section, we find that this setup avoided the slow RG flow of velocity, such that the finite-size simulations are closer to the nontrivial fixed point of the QCP. Second, the $1/\nu_{GN}$, η_ϕ in Tab. I are consistent with previous QMC results, and because finite-size effects have been efficiently suppressed in the present study, although our system sizes are only moderately large ($L = 14$), we can perform the crossing-point scaling to independently obtain $1/\nu_{GN}$, η_ϕ and the correction exponent ω , where the later cannot be accessed in the previous QMC simulations. Our fermionic anomalous dimension η_ψ is different from the the previous QMC result [22], and is significantly closer to the theory predictions from perturbative RG and conformal bootstrap. In our previous QMC work [21], the η_ψ couldn't be obtained through the fitting formula shown in Eq. (9), precisely because the strong finite-size effect in the simulation renders the slow (logarithmic) RG flow and consequently the Green's function data at finite sizes cannot produce a robust value of η_ψ . Therefore we are more confident with η_ψ obtained in this work. In fact, the exponents reported here, $\{1/\nu_{GN}, \eta_\phi, \eta_\psi, \omega\}$ offer the most complete set of numerically measured critical exponents till now for the $N_f = 8$ chiral Ising GN transition. Thanks to the careful model design, these results provide the much needed benchmark for future numerical and analytical investigations.

B. Velocities at transition point

As have been mentioned above, our designer Hamiltonian enjoys the advantage of maintaining the Lorentz symmetry even at the bare level, i.e., the linear dispersion region of both fermion and boson are enlarged in the BZ and their velocities are made identical by choosing suitable values of t_1 and J_1 . With such optimization, finite-size effects at the chiral Ising GN QCP are reduced and thus the exponents converges to stable values even with just moderately large system sizes up to $L = 14$. To further verify whether the fermion and boson velocities indeed remain identical and maintain their

bare values, here we directly measure these two velocity at the chiral Ising GN QCP.

Here, we measure the velocities via the dynamical Green's functions (the dynamical fermionic and bosonic propagators) $G^f(\mathbf{k}, \tau) = \langle c^\dagger(\mathbf{k}, \tau)c(\mathbf{k}, 0) \rangle$ and $G^b(\mathbf{q}, \tau) = \langle \phi(\mathbf{q}, \tau)\phi(-\mathbf{q}, 0) \rangle$. In the projector QMC, these two Green's functions are readily obtained from the imaginary time correlation functions [29, 30]. Since both fermion and boson have two sublattices, we measure the trace of the 2×2 matrices at each momentum point, and from fitting the imaginary time decay of $G(\mathbf{k}, \tau) \propto e^{-\Delta(\mathbf{k})\tau}$, the many-body excitation gaps are obtained at each momenta \mathbf{k} and \mathbf{q} . This relation between the excitation gap and the momentum marks the "mass shell", in analogy to the relativistic quantum field theory. Then we fit this relation near the Dirac point $\mathbf{K} = (\pi, 0)$ for fermions and near the Γ point $\mathbf{Q} = (0, 0)$ for bosons as $\Delta_f \sim v_f(\mathbf{k} - \mathbf{K})$ and $\Delta_b \sim v_b(\mathbf{k} - \mathbf{Q})$ respectively. This is how the velocities at the strong-coupling fixed point are obtained.

The results are shown in Figs. 1 (d) and (e). With system size up to $L = 14$, we find that v_f is very close to its bare value with very good linear behavior and v_b is also close to its bare value with slightly larger error-bars and deviations. This is due to the fact that our boson is a continuous field and the Monte Carlo moves, even with non-local SLMC update scheme, still suffers from the slow Monte Carlo dynamics and rendering slightly worse data quality. But, nevertheless, the results of v_f and v_b are indeed identical within error bars at the chiral Ising GN QCP. This result confirms the absence of the slow velocity RG flow, which helps control the finite-size effect in our simulations.

C. Conductivity

With the basic scaling properties of the $N_f = 8$ chiral Ising GN QCP determined, we can now pursue more sophisticated properties of this fermionic QCP, e.g. the conductivity. In condensed matter physics, conductivity is one of the most important physical quantities for both the theoretical and experimental studies. However, systematic studies of the scaling behavior of the conductivity at the close vicinity of a fermionic quantum critical point remains a challenging topic. In partic-

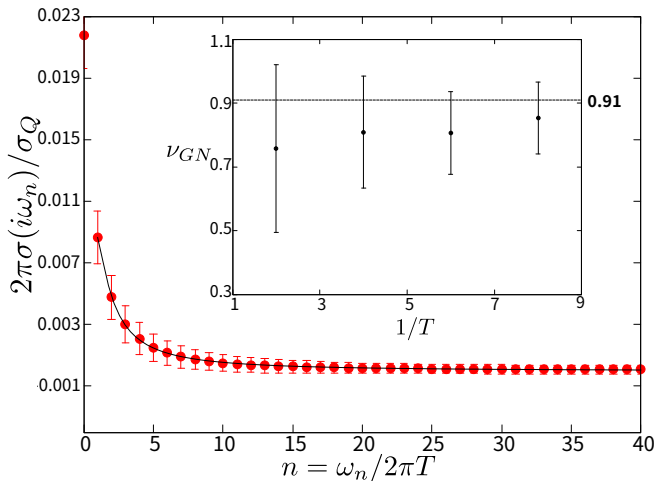


FIG. 5. The Matsubara frequency dependence of the conductivity at the critical point $m = m_c^*$ and finite temperature with $\beta \propto L$. The solid line is the fitting to the conformal theory prediction [Eq. (10)], which gives rise to the correlation length exponent ν_{GN} at the limit of $\omega_n \gg T$. The inset shows the extrapolation of the fitted ν_{GN} with decreasing temperature $1/T$, and the obtained value is well consistent with that shown in Tab. I indicated by the dashed line in the inset.

ular, for large-scale numerical simulations of Dirac fermion QCPs, the scaling behavior of the conductivity remains largely an uncharted area, so does its connections with the conformal field theoretical understanding of the problem [37]. It has been proposed and demonstrated in bosonic quantum $O(2)$ models at the Wilson-Fisher fixed point [37–39] that the finite temperature and frequency optical conductivity obeys a scaling law that are related with the QCP at zero temperature. In particular, the following generic form is expected

$$\begin{aligned} \frac{\sigma(i\omega_n)}{\sigma_Q} &= -\frac{1}{\omega_n} \langle J_x(\omega_n) J_x(-\omega_n) \rangle + \dots \\ &= \sigma_\infty + b_1 \left(\frac{T}{\omega_n}\right)^{3-1/\nu_{GN}} + b_2 \left(\frac{T}{\omega_n}\right)^3 + \dots, \quad (10) \\ &\text{at } \omega_n \gg T \end{aligned}$$

where $\sigma(i\omega_n)$ is the conductivity at the Matsubara frequency $\omega_n = 2\pi nT$, and $\sigma_Q = \frac{(e^*)^2}{h}$ is the quantum unit of conductance with e^* the effective charge in the model such that σ/σ_Q becomes dimensionless. σ_∞ is the limiting value of conductivity at $T \rightarrow 0$, b_1 and b_2 are coefficient related with the operator product expansion of the current operators in terms of other operators of the chiral Ising GN CFT and can in principle be estimated at large N limit. Coefficients at bosonic $O(N)$ Wilson-Fisher CFT have been estimated at large N [37], but those at fermionic QCPs such as the current one have not been calculated to the best of our knowledge.

Nevertheless, the conformal symmetry provides to us the scaling behavior of Eq. (10), which can be used to independently verify the correlation length exponent ν_{GN} and compare with the value obtained from crossing point analysis in Sec. III A. The current operator $J_x(\omega_n)$ in Eq. (10) is the Fourier transformation of $J_x(\mathbf{r}_i, \tau) = -it \langle (c^\dagger(\mathbf{r}_i, \tau) c(\mathbf{r}_{i+\hat{x}}, \tau) -$

$c^\dagger(\mathbf{r}_{i+\hat{x}}, \tau) c(\mathbf{r}_i, \tau)) \rangle$ where \hat{x} denotes the current along the x -direction of the lattice. We note that here \hat{x} or \hat{y} directions are equivalent due to the four-fold rotational symmetry, and thus can be symmetrized in the simulation to increase the data quality.

The measured conductivity is shown in Fig. 5, where the conductivity of a $L = 10$ system at the critical point m_c^* and temperature $T = 1/8$ is presented in the main panel. After fitting the decay with the form of Eq. (10), we find $2\pi \frac{\sigma(i\omega_n)}{\sigma_Q} = \sigma_\infty + 0.0337/n^{1.8175} - 0.043/n^3$ and the corresponding $\nu_{GN} = 0.85(11)$. Then we perform the same simulation at a few other temperatures and extrapolate the obtained ν_{GN} as a function of $1/T$, to satisfy the limit $\omega_n \gg T$ (the inset of Fig. 4). The dashed line in the inset indicates the value of ν_{GN} obtained in Tab. I, and it is clear that as temperature is decreasing, the ν_{GN} obtained from the fitting of critical conductivity with Eq. (10) are well consistent with the value obtained in previous sections. Such consistency implies that on the one hand our critical exponent ν_{GN} is robust (with three independent ways of obtaining it via U , R and σ), and on the other the critical conductivity at finite frequency can indeed be used to obtain the critical exponent of fermionic QCP, even though the conformal field theory description of this QCP is yet to be complete.

IV. CONCLUSION

Over the years, controlled study of fermionic QCPs is the question that have been haunting the minds of physicists in the field of strongly-correlated systems. Although extensive efforts have been devoted and great progress has been achieved, even greater challenges are still lying in front of the community. Among those, controlled analytical calculation of the critical properties and numerical approaches such that the computational complexity ($O(\beta N^3)$ for fermionic QMC for example) can be overcome and the thermodynamic limit can be safely reached, are the important steps towards the final solution of this challenging problem. For this objective, our efforts here focus on improving the situation at the numeric front, utilizing new techniques in model design guided by insights gained from the field theory studies.

The designer Hamiltonian that we have engineered realizes a lattice model of the $(2+1)d$ $N_f = 8$ Gross-Neveu (GN) chiral Ising transition of Dirac fermions coupled to critical bosonic modes. By extending the linear-dispersion region in the BZ, and engineer the fermion and boson dispersions in order to achieve identical velocities at the bare level, we find, via QMC simulations assisted with the SLMC of the non-local bosonic configurational moves, that the strongly-coupled Dirac fermions and critical Ising bosons still acquire the same velocity at the QCP. In other words, the designer model place the starting point of the RG flow close to the nontrivial fixed point, and consequently minimizes the finite size effects.

With these advances in model design and algorithm development, we could acquire robust critical exponents of GN chiral Ising transition with only moderately large system size upto $L = 14$, avoiding the heavy computational burden for pushing to larger sizes. In fact, we are able to obtain the complete set

of critical exponents $\{1/\nu_{\text{GN}}, \eta_\phi, \eta_\psi, \omega\}$ than previous works (including that of ourselves [21]) and therefore provide the much needed benchmark results for the further developments at the analytical front such as controlled RG calculation and conformal bootstrap analysis. We also calculated the conductivity at the QCP and find its finite frequency scaling behavior consistent with conformal field theory prediction. Our approach provides the promising direction towards the eventual controlled study of fermionic QCPs, and the same concept and principles can be easily generalized to other fermionic QCPs as well, such as the GN chiral XY [40] and Heisenberg [19, 23] and the fermion surface coupled to the critical bosons [17] and topological orders [41, 42]. Efforts along this line of thinking may help shed new light on key open questions in various fermionic QCPs and may eventually lead to their final solutions.

ACKNOWLEDGEMENT

We thank Michael Scherer, Lukas Jannsen, Joseph Maciejko, Andreas Läuchli, Thomas Lang, Stefan Wessel, Fakher Assaad and Xi Dai for insightful discussions on both the fermionic GN transitions and QMC methodologies, William Witczak-Krempa for enlightening conversations on the finite frequency conductivity at QCPs, and Ning Su and Junchen Rong for explanations on the conformal bootstrap estimation on the fermion QCPs. YZL and ZYM acknowledge the supports from the Ministry of Science and Technology of China through the National Key Research and Development Program (Grant No. 2016YFA0300502), the Strategic Priority Research Program of the Chinese Academy of Sciences (Grant No. XDB28000000), the National Science Foundation of China (Grant Nos. 11421092, 11574359, 11674370) and Research Grants Council of Hong Kong Special Administrative Region of China through 17303019. K.S. acknowledges support from the National Science Foundation under Grant No. EFRI-1741618. We thank the Center for Quantum Simulation Sciences in the Institute of Physics, Chinese Academy of Sciences, the Tianhe-1A platform at the National Supercomputer Center in Tianjin and Tianhe-2 platform at the National Supercomputer Center in Guangzhou for their technical support and generous allocation of CPU time.

Appendix A: Velocity estimations

In this section, we provide analytic calculations of the velocities of free fermion and boson of our model in Eq. (1).

Through Legendre transformation of L_{Fermion} , the fermionic H_{Fermion} can be written as

$$H_{\text{Fermion}} = \sum_{(ij),\sigma} -te^{-i\sigma\theta} c_{i,\sigma}^\dagger c_{j,\sigma} + h.c. \quad (\text{A1})$$

In the momentum space, through Fourier transformation, we

obtain

$$H_{\text{Fermion}} = -2t_1 \begin{pmatrix} 0 & A+B \\ A^*+B^* & 0 \end{pmatrix} - \frac{2t_1}{27} \begin{pmatrix} 0 & C+D \\ C^*+D^* & 0 \end{pmatrix}$$

where

$$\begin{aligned} A &= \cos\left[\frac{k_x}{2} + \frac{k_y}{2}\right] \exp\left[i\frac{\pi}{4}\right] \\ B &= \cos\left[\frac{k_x}{2} - \frac{k_y}{2}\right] \exp\left[-i\frac{\pi}{4}\right] \\ C &= \cos\left[\frac{3k_x}{2} + \frac{3k_y}{2}\right] \exp\left[i\frac{\pi}{4}\right] \\ D &= \cos\left[\frac{3k_x}{2} - \frac{3k_y}{2}\right] \exp\left[-i\frac{\pi}{4}\right] \end{aligned} \quad (\text{A2})$$

From the Eq. (A2), one sees the Dirac points are located in the $(\pi, 0)$ and $(0, \pi)$ in BZ which we then Taylor expand in the neighborhood of them,

$$H_{\text{Fermion}} = \frac{8}{9}\sqrt{2}t_1 \begin{pmatrix} 0 & -k_x - ik_y \\ -k_x + ik_y & 0 \end{pmatrix} \quad (\text{A3})$$

So the free fermion velocity $v_F = \frac{8}{9}\sqrt{2}t_1$ is deduced.

For the free boson which does not include the term of ϕ^4 , considering the following form of bosonic action,

$$S = \int dt \sum_i \frac{1}{4}(\partial_t \phi_i)^2 - \sum_{i,j} J_{ij}(\phi_i - \phi_j)^2 - \sum_i m\phi_i^2 \quad (\text{A4})$$

where J_1, J_2, J_3 and J_4 are given in Fig. 1 (c).

Again going to the momentum space via Fourier transformation, we obtain

$$\begin{aligned} S &= \sum_\omega \sum_q \left[\frac{1}{4}\omega^2 - 2J_1[(2 - \cos[q_x] - \cos[q_y])] \right. \\ &\quad \left. - \frac{1}{8}(2 - \cos[q_x] - \cos[q_y]) \right. \\ &\quad \left. + \frac{1}{63}(2 - \cos[q_x] - \cos[q_y]) \right. \\ &\quad \left. - \frac{1}{896}(2 - \cos[q_x] - \cos[q_y]) - m \right] \phi_{q,w}^2 \end{aligned} \quad (\text{A5})$$

The Euler-Lagrange's equation require $S = 0$ which provide the stationary solution for bosonic field ϕ

$$\begin{aligned} \frac{1}{4}\omega^2 &= 2J_1[(2 - \cos[q_x] - \cos[q_y]) - \frac{1}{8}(2 - \cos[q_x] - \cos[q_y]) + \\ &\quad \frac{1}{63}(2 - \cos[q_x] - \cos[q_y])] - \\ &\quad \frac{1}{896}(2 - \cos[q_x] - \cos[q_y]) + m \end{aligned} \quad (\text{A6})$$

close to $\mathbf{Q} = (0, 0)$, the dispersion is

$$\omega = \pm 2\sqrt{\frac{5J_1}{8}(q_x^2 + q_y^2) + m} \quad (\text{A7})$$

So the velocity of boson is $v_b = 2\sqrt{5J_1/8}$.

The condition $v_F = v_b$ require the relation of $J_1 = 0.6320t_1^2$.

Appendix B: projective QMC and SLMC

As mention in the main text, we employ the projective QMC [21] to solve the model in Eq. (1). In the QMC simulation, the partition function is written as

$$Z = \langle \Phi_T | \exp(-2\Theta H) | \Phi_T \rangle = \sum_{\{\phi\}} W_{\text{Boson}} \prod_{\sigma=\uparrow,\downarrow} \det(P_\sigma^\dagger B_m^\sigma \cdots B_1^\sigma P_\sigma), \quad (\text{B1})$$

where Θ plays the role of inverse temperature and $\phi_{\tau,i}$ is the bosonic field at imaginary time τ and site i . For the bosonic part of the configurational weight, the weight W_{Boson} is of the form

$$W_{\text{Boson}} = \exp[-\Delta\tau \left(\sum_{i,\tau} \frac{1}{4\Delta\tau^2} (\phi_{i,\tau+1} - \phi_{i,\tau})^2 + \sum_{i,j} \sum_{\tau} V_{ij,\tau} \right)], \quad (\text{B2})$$

where $V_{ij,\tau} = J_{ij}(\phi_{i,\tau} - \phi_{j,\tau})^2 + m\phi_{i,\tau}^2$

For the fermion determinant, $|\Phi_T\rangle$ is the trial wave function which is comprised of the eigenvectors of the free fermion Hamiltonian for the occupied states, represented by a P_σ matrix with size $N \times 2N$ where N is the number of electrons at the half-filling. B_τ^σ matrix at time slice τ is then

$$B_\tau^\sigma = \exp(-\Delta\tau(H_{\text{Fermion}} + H_{\text{Coupling}})) = \exp(-\Delta\tau H_{\text{Fermion}}) \exp(-\Delta\tau H_{\text{Coupling}}). \quad (\text{B3})$$

Let's now compute the ratio for the fermion determinant for the QMC update. Introduce the notation $B(\tau_1, \tau_2) = B_{\tau_1}^\sigma \cdots B_{\tau_2+1}^\sigma$, $B^< = P_\sigma^\dagger B(2\Theta, \tau)$ and $B^> = B(\tau, 0)P_\sigma$, one has

$$W_{\text{Fermion}} = \det[B^< B^>], \quad (\text{B4})$$

where the Green's function is

$$1 - G(\tau) = B^> (B^< B^>)^{-1} B^< \quad (\text{B5})$$

The local update of determinant QMC suffers from the critical slowing-down close to the QCP, to overcome this problem, we make use of the recently developed self-learning Monte Carlo (SLMC) [25, 26] scheme to perform more efficient Monte Carlo moves in the configurational space. The core idea of SLMC is to obtain the low-energy effective bosonic Hamiltonian of the problem at hand, and this can be achieved by training an effective model from the configurations saved in a small lattice obtained from the conventional determinant QMC simulation. In our case, the Lagrangian of effective model is of the following form

$$L = L_{\text{Boson}} + L_{\text{eff}} \quad (\text{B6})$$

with

$$L_{\text{Boson}} = \sum_p \left[\frac{1}{4} \left(\frac{\partial \phi_p}{\partial \tau} \right)^2 + m\phi_p^2 + \phi_p^4 \right] + \sum_{(p,q)} J_{pq} (\phi_p - \phi_q)^2, \quad (\text{B7})$$

$$L_{\text{eff}} = J_k^{\text{eff}} \sum_i \lambda_i \phi_{i\tau} + \sum_{(ij,n)} J_n^{\text{eff}} \phi_{i\tau} \phi_{j\tau}$$

The spirit of the learning process is to replace the effect of L_{Fermion} and L_{Coupling} with L_{eff} . λ_i take value of ± 1 which has opposite signs in two bosonic sublattices. J_k^{eff} and J_n^{eff} -s (the n th-nearest interaction between the bosons) are the trained effective couplings which is shown in Tab II from a $L = 6$ systems at $m = -0.06$ and $\Theta = 2L$. With the trained L_{eff} and the bare boson L_{Boson} , one can then use the Lagrangian in Eq. (B6) to guide the Monte Carlo move of the boson fields and only after substantially many such updates, evaluate the fermion determinant in Eq. (B1) to respect the detailed balance condition of the original model in Eq. (1). For more detailed description of SLMC, the assiduous readers are referred to the Refs. [18, 25, 26].

One more obstacle particularly associated with the current problem is that for training the effective model, the calculation of the fermion determinant is necessary, but the $\det[B^< B^>]$ can be very large (as large as e^{2000}) in our model. To overcome such numerical difficulty, we note that the real important quantity we need to calculate is $\log(\det[B^< B^>])$ in the SLMC scheme [26]. If the $\det[B^< B^>]$ is divided into product of several parts (such as $T = A_1 A_2 A_3$), then the large value in the determinant can be broken into sum several small parts (eg. $\log \det[T] = \log \det[A_1] + \log \det[A_2] + \log \det[A_3]$), where each part is small enough to be handled numerically, i.e.,

$$\det[P^\dagger B_s(2\Theta, 0)P] = \det[P^\dagger B^n B^{n-1} \cdots B^2 B^1 P], \quad (\text{B8})$$

the UDV decomposed can be used in the model

$$B^> = U^> D V \quad (\text{B9})$$

where $U^>$ is a rectangular matrix $2N \times N$ and D contains the N eigenvalues of scale from large to small and V is an upper unit triangular matrix $N \times N$. In this way, we can obtain

$$\begin{aligned} & \det[P^+ B^n B^{n-1} \cdots B^2 B^1 P] \\ &= \det[P^+ B^n B^{n-1} \cdots B^2 B^1 P] \\ &= \det[P^+ B^n B^{n-1} \cdots B^2 U_1^> D^1 V^1] \\ &= \det[P^+ B^n B^{n-1} \cdots U_2^> D^2 V^2 D^1 V^1] \\ &\cdots \\ &= \det[P^+ U_n^> D^n V^n D^{n-1} V^{n-1} \cdots D^2 V^2 D^1 V^1] \\ &= \det[P^+ U_n^>] \det[D^n D^{n-1} D^{n-2} \cdots D^2 D^1] \det[V^n V^{n-1} \cdots V^2 V^1], \end{aligned} \quad (\text{B10})$$

such that we can break the determine into three parts and compute the weight accordingly.

With the determinant weight obtained for small system sizes, we can train and obtain the parameters for the effective model. As the example shown in Tab. II, one can see that interactions of several different distances $J_{1,2,3}^{\text{eff}}$ are all important as they have the same scale. With the cumulative update [26] in SLMC, it turns out that the simulation with such effective model but applied to $L \geq 6$ systems, are sampled with shorter equilibrium time compared with conventional determinant QMC.

J_k^{eff}	J_1^{eff}	J_2^{eff}	J_3^{eff}
-0.0143045485581	-0.205175906625	-0.0539032527282	-0.111523376999

TABLE II. Fitted values of J_k^{eff} , J_1^{eff} , J_2^{eff} and J_3^{eff} when $m = -0.06$ for $L = 6$ system at $\Theta = 2L$.

- [1] J. A. Hertz, *Phys. Rev. B* **14**, 1165 (1976).
- [2] A. J. Millis, *Phys. Rev. B* **48**, 7183 (1993).
- [3] T. Moriya, *Spin Fluctuations in Itinerant Electron Magnetism* (Springer-Verlag Berlin Heidelberg, 1985).
- [4] A. Abanov, A. V. Chubukov, and J. Schmalian, *Advances in Physics* **52**, 119 (2003).
- [5] A. V. Chubukov, C. Pépin, and J. Rech, *Phys. Rev. Lett.* **92**, 147003 (2004).
- [6] A. V. Chubukov and D. L. Maslov, *Phys. Rev. Lett.* **103**, 216401 (2009).
- [7] S.-S. Lee, *Phys. Rev. B* **80**, 165102 (2009).
- [8] M. A. Metlitski and S. Sachdev, *Phys. Rev. B* **82**, 075127 (2010).
- [9] M. A. Metlitski and S. Sachdev, *Phys. Rev. B* **82**, 075128 (2010).
- [10] A. Schliep, P. Lunts, and S.-S. Lee, *Phys. Rev. X* **7**, 021010 (2017).
- [11] A. W. Sandvik, *AIP Conference Proceedings* **1297**, 135 (2010), <https://aip.scitation.org/doi/pdf/10.1063/1.3518900>.
- [12] Y. Schattner, S. Lederer, S. A. Kivelson, and E. Berg, *Phys. Rev. X* **6**, 031028 (2016).
- [13] X. Y. Xu, K. Sun, Y. Schattner, E. Berg, and Z. Y. Meng, *Phys. Rev. X* **7**, 031058 (2017).
- [14] M. H. Gerlach, Y. Schattner, E. Berg, and S. Trebst, *Phys. Rev. B* **95**, 035124 (2017).
- [15] Z. H. Liu, X. Y. Xu, Y. Qi, K. Sun, and Z. Y. Meng, *Phys. Rev. B* **98**, 045116 (2018).
- [16] Z. H. Liu, X. Y. Xu, Y. Qi, K. Sun, and Z. Y. Meng, *Phys. Rev. B* **99**, 085114 (2019).
- [17] Z. H. Liu, G. Pan, X. Y. Xu, K. Sun, and Z. Y. Meng, *Proceedings of the National Academy of Sciences* **116**, 16760 (2019).
- [18] X. Y. Xu, Z. H. Liu, G. Pan, Y. Qi, K. Sun, and Z. Y. Meng, *Journal of Physics: Condensed Matter* **31**, 463001 (2019).
- [19] N. Zerf, L. N. Mihaila, P. Marquard, I. F. Herbut, and M. M. Scherer, *Phys. Rev. D* **96**, 096010 (2017).
- [20] B. Ihrig, L. N. Mihaila, and M. M. Scherer, *Phys. Rev. B* **98**, 125109 (2018).
- [21] Y.-Y. He, X. Y. Xu, K. Sun, F. F. Assaad, Z. Y. Meng, and Z.-Y. Lu, *Phys. Rev. B* **97**, 081110 (2018).
- [22] S. Chandrasekharan and A. Li, *Phys. Rev. D* **88**, 021701 (2013).
- [23] T. C. Lang and A. M. Läuchli, *Phys. Rev. Lett.* **123**, 137602 (2019).
- [24] M. Schuler, S. Hesselmann, S. Whitsitt, T. C. Lang, S. Wessel, and A. M. Läuchli, arXiv e-prints, arXiv:1907.05373 (2019), arXiv:1907.05373 [cond-mat.str-el].
- [25] J. Liu, Y. Qi, Z. Y. Meng, and L. Fu, *Phys. Rev. B* **95**, 041101 (2017).
- [26] X. Y. Xu, Y. Qi, J. Liu, L. Fu, and Z. Y. Meng, *Phys. Rev. B* **96**, 041119 (2017).
- [27] Y. Otsuka, S. Yunoki, and S. Sorella, *Phys. Rev. X* **6**, 011029 (2016).
- [28] S. Weinberg, *The quantum theory of fields* (Cambridge University Press, 2005).
- [29] F. Assaad and H. Evertz, “World-line and determinantal quantum monte carlo methods for spins, phonons and electrons,” in *Computational Many-Particle Physics*, edited by H. Fehske, R. Schneider, and A. Weiße (Springer Berlin Heidelberg, Berlin, Heidelberg, 2008) pp. 277–356.
- [30] Z. Y. Meng, T. C. Lang, S. Wessel, F. F. Assaad, and A. Muramatsu, *Nature* **464** (2010), 10.1038/nature08942.
- [31] L. Iliesiu, F. Kos, D. Poland, S. S. Pufu, and D. Simmons-Duffin, *Journal of High Energy Physics* **2018**, 36 (2018).
- [32] J. Rong and N. Su, arXiv e-prints, arXiv:1807.04434 (2018), arXiv:1807.04434 [hep-th].
- [33] K. Binder, *Zeitschrift für Physik B Condensed Matter* **43**, 119 (1981).
- [34] S. Pujari, T. C. Lang, G. Murthy, and R. K. Kaul, *Phys. Rev. Lett.* **117**, 086404 (2016).
- [35] H. Shao, W. Guo, and A. W. Sandvik, *Science* **352**, 213 (2016).
- [36] Y. Q. Qin, Y.-Y. He, Y.-Z. You, Z.-Y. Lu, A. Sen, A. W. Sandvik, C. Xu, and Z. Y. Meng, *Phys. Rev. X* **7**, 031052 (2017).
- [37] E. Katz, S. Sachdev, E. S. Sørensen, and W. Witczak-Krempa, *Phys. Rev. B* **90**, 245109 (2014).
- [38] K. Chen, L. Liu, Y. Deng, L. Pollet, and N. Prokof'ev, *Phys. Rev. Lett.* **112**, 030402 (2014).
- [39] A. Lucas, S. Gazit, D. Podolsky, and W. Witczak-Krempa, *Phys. Rev. Lett.* **118**, 056601 (2017).
- [40] Y. Da Liao, Z. Y. Meng, and X. Y. Xu, *Phys. Rev. Lett.* **123**, 157601 (2019).
- [41] C. Chen, X. Y. Xu, Y. Qi, and Z. Y. Meng, arXiv e-prints, arXiv:1904.12872 (2019), arXiv:1904.12872 [cond-mat.str-el].
- [42] S. Gazit, F. F. Assaad, and S. Sachdev, arXiv e-prints, arXiv:1906.11250 (2019), arXiv:1906.11250 [cond-mat.str-el].